Available online at www.sciencedirect.com

ScienceDirect

Underground Space 27 (2026) 301–320

www.keaipublishing.com/undsp

Research Paper

In situ, non-destructive and rapid mineral mapping in tunnels with hyperspectral imaging

Shan Li [a,b], Peng Lin [a,b], Kai Yang [a,b], Zhenhao Xu [a,b,*]

[a] *State Key Laboratory for Tunnel Engineering, Institute of Geotechnical and Underground Engineering, Shandong University, Jinan 250061, China*
[b] *School of Qilu Transportation, Shandong University, Jinan 250061, China*

Received 16 June 2025; received in revised form 3 November 2025; accepted 8 November 2025
Available online 01 February 2026

Abstract

Hyperspectral imaging provides a novel approach for intelligent geological perception in tunnelling and underground engineering due to its high spectral resolution, nondestructive nature, and combined spectral-spatial information. However, in confined underground spaces, noise is often introduced by short exposure times, low illumination, and dust, and limited spatial resolution can cause mixed pixel effects, complicating data processing. This study presents an underground hyperspectral imaging-based mineral mapping method that achieves wall-rock visualization and semi-quantitative mineral mapping through image denoising and spectral unmixing. A spatial-spectral recurrent transformer U-Net is developed to reduce noise by leveraging spectral band correlations and nonlocal spatial-texture dependencies. A Dirichlet-based mixed pixel simulation is used to address spectral mixing, with the N-FINDR algorithm identifying endmember minerals, and the fully constrained least squares method to estimate mineral abundances. When applied to a water diversion tunnel in Shanxi, the method generates spatial distribution maps of dolomite and calcite. The experimental results confirm its effectiveness for intelligent geological logging and subsurface geological feature analysis.

Keywords: Hyperspectral imaging; Underground space; Geological analysis; Mineral mapping; Hyperspectral noise reduction; Hyperspectral unmixing

1 Introduction

Tunnel construction frequently passes through unfavorable geological zones, including faults, karst, and hydrothermal alteration zones (Deng et al., 2023; Lu et al., 2023; Zhang et al., 2023). Such conditions often cause major geological disasters, such as water inrushes, mud outbursts, machine jamming, and landslides, posing serious threats to construction safety (Liu et al., 2025). Geological analysis constitutes the fundamental method for identifying adverse geological conditions in tunnels and offers intuitive, reliable, and widely applicable assessments. Other identification approaches are fundamentally predicated on geological analysis and judgment, making geological analysis the cornerstone for enhancing the identification accuracy in adverse tunnel geology (Klose et al., 2007; Liu et al., 2023). Consequently, accurate, reliable, and intelligent geological analyses are critical for ensuring tunnel safety during rapid construction (Akgün et al., 2014; Bhasin et al., 1995; X. Wang et al., 2024).

Geological analysis encompasses the assessment of mineral composition in wall rocks, where the mineral composition critically governs the physical and mechanical properties of the tunnel wall rock. Variations in the mineral composition can induce substantial differences in the engineering properties of rock masses. Taking clay minerals as an example, their low frictional strength and directional arrangement characteristics weaken the mechanical properties of fault zones. Simultaneously, mineralization

* Corresponding author at: State Key Laboratory for Tunnel Engineering, Institute of Geotechnical and Underground Engineering, Shandong University, Jinan 250061, China.
E-mail address: zhenhao_xu@sdu.edu.cn (Z. Xu).
Peer review under the responsibility of Tongji University

https://doi.org/10.1016/j.undsp.2025.11.003

reduces rock mechanical strength, potentially triggering geological disasters such as tunnel deformation and sudden water/mud inrushes (Xu et al., 2023). Zhou et al. (2014) investigated the mechanical behavior of water diversion tunnels by analyzing the physical properties and mineral composition of chlorite schists, providing a comprehensive stability evaluation. Xu et al. (2022) developed a fault identification method that integrates rock microstructure, geochemistry, and mineralogy using optical microscopy, X-ray fluorescence (XRF), and X-ray diffraction (XRD). Applied to the tunnel boring machines (TBM) 2 segment of the Yellow River Diversion Tunnel Project in central Shanxi, China, it proved effective for comprehensive fault layer identification in underground and mining engineering, as well as geological analysis of TBM jamming. Y. Wang et al. (2024) proposed a rock quartz content prediction method combining Laser-induced breakdown spectroscopy (LIBS), rock chemical analysis, and artificial intelligence algorithms, providing references for tunnel TBM construction and enabling an advanced understanding of rock characteristics. These studies demonstrate that refined and quantitative in situ rock and mineral analysis in tunnels can elucidate the mineral composition and spatial structural patterns within tunnel rock masses, thereby underpinning research on adverse geology, such as faults and alteration zones.

Conventional mineral identification methods for rocks primarily include microscopic analysis, XRD, and infrared spectral analyses (H. Zhang et al., 2025). Microscopic thin-section identification can reveal mineral microcharacteristics and structures in detail (Yang et al., 2024); however, its utility is limited by stringent laboratory requirements and the necessity for rock sample thin-section preparation, rendering it unsuitable for rapid construction. XRD technology analyzes the crystal structure and composition through crystalline diffraction phenomena (Ali et al., 2022); nevertheless, it requires destructive sample preparation steps such as collection, grinding, and processing, which are cumbersome and incompatible with rapid, large-scale in situ mineral identification requirements. Atomic spectroscopic analysis performs qualitative and quantitative analyses based on atomic spectral line behavior and intensity characteristics (McElderry et al., 2013), yet it involves time-consuming sample preparation and testing and fails to satisfy large-area rapid testing demands. In recent years, as tunnel construction has progressed toward intelligence, the requirements for intelligent geological analyses have correspondingly increased. To address the current intelligent construction needs, this study contends that rock and mineral testing technology must evolve to meet the following criteria: (1) be rapid and near real-time to support automated and intelligent construction; (2) operate in situ and remotely without sample contact or damage; (3) have simple and efficient procedures; and (4) exhibit high autonomy and intelligence.

Hyperspectral technology is a nondestructive, rapid, and in situ approach for physical property detection by leveraging material composition (Bhargava et al., 2024; Zahiri et al., 2022). Each material exhibits a unique spectral signature, which enables feature identification (Peng et al., 2025). Compared with conventional techniques, this technology offers superior efficiency, reduced labor requirements, and high accuracy, rendering it widely applicable across scientific research and industrial applications (Huang et al., 2024). When hyperspectral technology acquires reflectance spectral data from rock minerals (under illumination at specific wavelengths), the minerals undergo electronic and molecular vibrational transitions under the electromagnetic radiation, exhibiting distinct spectral characteristics within specific electromagnetic bands. Mineral spectral studies indicate that rock minerals exhibit a series of diagnostic spectral features between 0.4 and 2.5 μm. These absorption characteristics arise from electronic transitions of metal ions and the vibrations of molecular groups such as Al-OH, Mg-OH, and CO_3^{2-}. For instance, the absorption feature at 2.20 μm in muscovite stems from the stretching vibration of the Al-OH bond; kaolinite's dual absorption features at 2.20 and 2.16 μm serve as diagnostic markers; while absorption around 2.33 and 2.55 μm in carbonate minerals (such as calcite) relates to CO_3^{2-} ions. Consequently, spectral characteristics serve as proxies for rock composition and structure, thus enabling mineralogical identification (Chen et al., 2023; Zhao et al., 2018). Hyperspectral imaging integrates machine vision with spectroscopy, enabling simultaneous non-contact acquisition of spatial and spectral information. This capability has enabled its broad deployment in large-scale geological surveys, environmental monitoring, and mineral exploration (Son et al., 2022; Wang et al., 2025). Building upon open-air hyperspectral remote sensing and reflectance spectroscopy, rapid nondestructive in situ hyperspectral imaging technology presents a novel approach for intelligent geological logging in tunnel environments.

Underground environments pose significant challenges for hyperspectral analysis because of poor illumination, high humidity, and restricted access. To date, only a few studies have addressed hyperspectral data acquisition in underground mines. Lobo et al. (2021) employed a Specim FX17 (0.9–1.7 μm) hyperspectral camera under simulated tunnel lighting, demonstrating hyperspectral imaging for mapping tin-tungsten ore distributions on mine faces. Baik et al. (2023) developed a 3D hyperspectral scanning system to detect iron ores and assessed the effects of dust, water vapor, and vibration. Both operate under controlled conditions, whereas the actual acquisition suffers from short exposure, platform vibration, low light, and dust, which degrade the image quality. Moreover, limited spatial resolution and multi-mineral rock compositions often produce mixed spectra (Shah et al., 2025; Tao et al., 2024),

necessitating mineral decomposition and abundance quantification.

This study conducts in situ tunnel hyperspectral detection and proposes a geological analysis framework that enables wall-rock visualization and quantitative mineral mapping. A spatial-spectral recurrent transformer within a U-Net reduces noise by exploiting spectral correlations and nonlocal textures. Mixed spectra were simulated using a Dirichlet distribution, and spectrally pure endmembers were extracted via N-FINDR and unmixed with fully constrained least squares (FCLS) to estimate mineral abundances. This method maps the dolomite and calcite distributions to a water diversion tunnel in Shanxi, China. Spectral reconstruction yielded root mean square errors (RMSE) of 0.009 500, 0.011 858, 0.006 600, and 0.052 600 across regions, validating hyperspectral remote sensing as an effective tool for intelligent geological logging and subsurface geological characterization.

2 Mineral quantitative inversion method based on tunnel hyperspectral images

The mineral quantitative inversion method based on tunnel hyperspectral imagery, schematically illustrated in Fig. 1, incorporates two primary techniques: hyperspectral image noise reduction and spectral unmixing. This approach employs a deep learning model integrating recurrent neural networks (RNNs) (Liu et al., 2018) and Transformer (Ghosh et al., 2022) architectures to effectively suppress noise in complex tunnel environments, thereby enhancing signal-to-noise ratios. To address the spectral mixing phenomenon, a Dirichlet distribution-based mixed-pixel simulation method was developed. Subsequently, the N-FINDR algorithm (Wu et al., 2012) was applied to extract the mineral endmembers, followed by the solution of a linear mixing model via the FCLS (Wang et al., 2013) method to achieve quantitative mineral analysis. This process generates mineral spatial distribution maps, enabling nondestructive, in situ, and rapid mineralogical analyses of tunnel faces.

2.1 Tunnel hyperspectral image acquisition

This study established a hyperspectral imaging system for tunnel environments. A tripod-mounted hyperspectral camera (10 nm resolution, 1000–2500 nm range) was positioned on the tunnel face to capture the surrounding rock. The swing-scanning platform, camera, and two 1 kW halogen lamps were powered by a tunnel supply, with the lamps placed symmetrically for uniform illumination and warmed

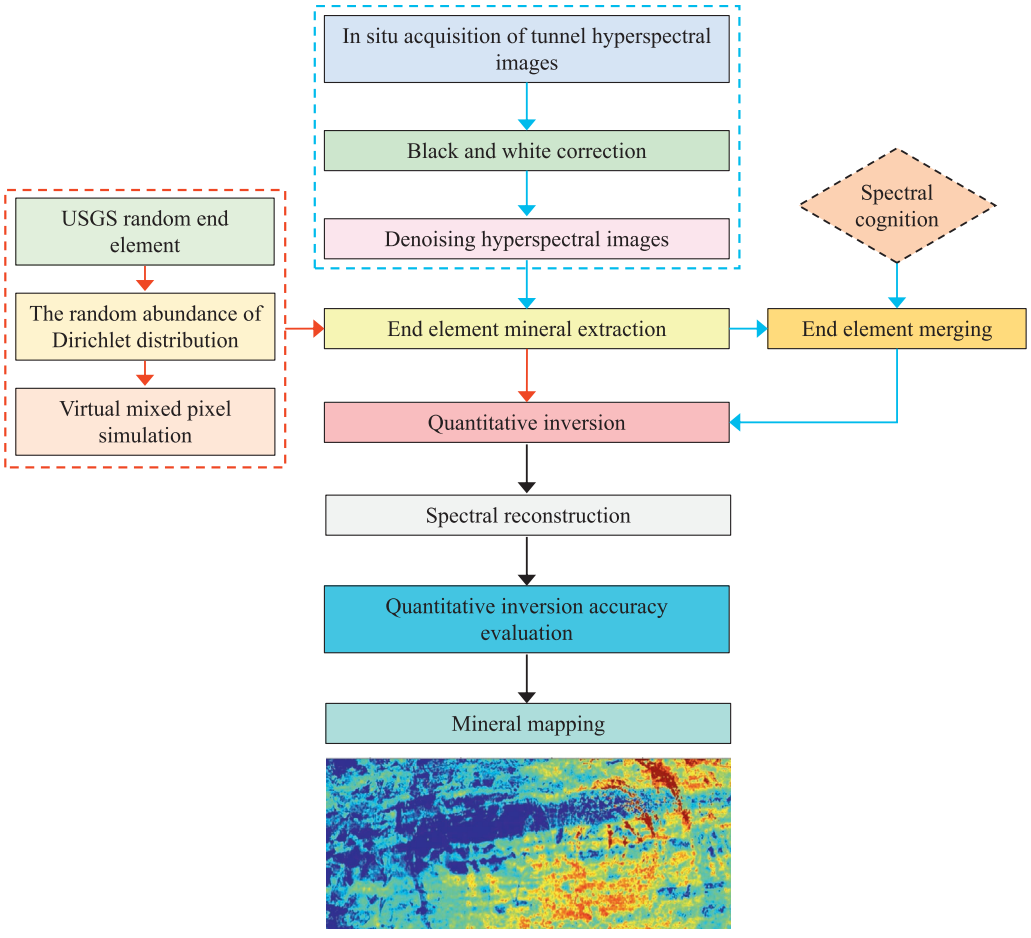

Fig. 1. Flowchart of mineral quantitative inversion technology for tunnel hyperspectral images.

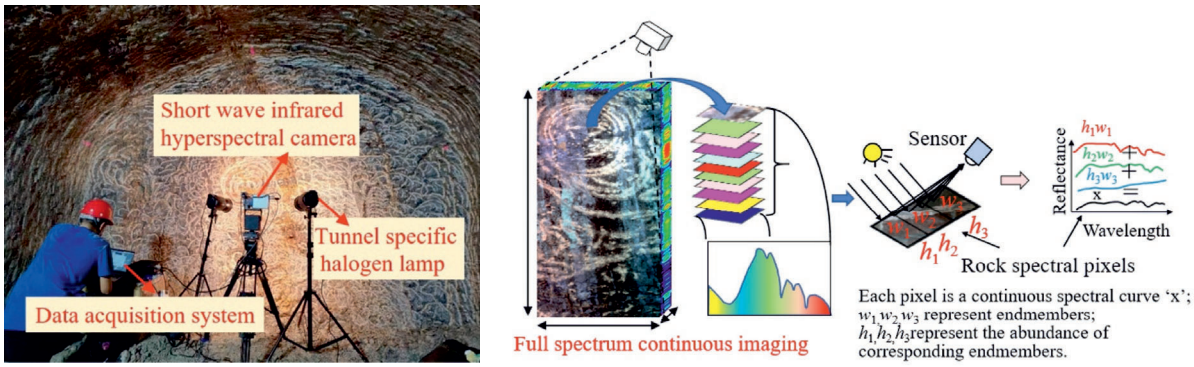

(a) (b)

Fig. 2. In situ hyperspectral image acquisition of tunnel. (a) Hyperspectral acquisition system (Xu et al., 2025b), and (b) hyperspectral image of wall rock.

for 10 min. White reference and dark current data were collected, the scanning speed and camera settings were adjusted to the target distance, and hyperspectral imaging was performed. The radiance data were preprocessed and converted into reflectance data (Fig. 2(a)). After calibrating light intensity, focal length, and scan speed, dark current data were collected, followed by spectral calibration using a Lambertian reference panel (≥99% reflectance) placed in the target area. Radiometric correction via black and white correction (Guo et al., 2025) was applied to the raw data, and the spectra were corrected using Eq. (1) to mitigate sensor noise and environmental effects and ensure accurate reflectance measurements.

$$R = \frac{I_{\text{raw}} - I_{\text{dark}}}{I_{\text{white}} - I_{\text{dark}}}, \tag{1}$$

where R represents the spectral reflectance of the sample after the black and white correction, I_{raw} is the spectral intensity of the rock reflection, I_{dark} is the dark-field spectrum obtained by covering the lens, and I_{white} is the spectral intensity reflected by the standard calibration whiteboard.

During hyperspectral remote sensing data acquisition, sensor spatial resolution limitations frequently cause individual pixels to encompass multiple rock and mineral components. Consequently, their spectral signatures superimpose, resulting in composite spectra where pixel-level reflectance curves no longer represent a single mineral species, but rather constitute weighted combinations of multiple endmember spectra at varying proportions (Fig. 2(b)).

2.2 Tunnel hyperspectral noise reduction

2.2.1 Network framework

In the field of geological hyperspectral imaging in tunnel engineering, this study introduces a U-shaped hyperspectral imagery (HSI) noise reduction framework based on deep learning to address the impact of noise on data quality in complex environments. This framework is based on the classic noise pollution model and assumes a clean tunnel hyperspectral image, as in $X \in \mathbb{R}^{H\times W\times \lambda}$, where H and W represent the height and width of the hyperspectral image, respectively, and λ represents the number of spectral bands. In the actual acquisition process, when remote sensing images are inevitably affected by noise N (e.g., Gaussian noise, pulse noise, and stripe noise) (Bu et al., 2025; T. Zhang et al., 2025), the collected hyperspectral image Y containing noise is represented as $Y = X + N$. This model aims to achieve noise reduction in in situ hyperspectral images in tunnels by learning the mapping relationship between the noisy hyperspectral image Y and clean hyperspectral image X.

This framework includes a shallow feature extraction module, multi-scale encoder-decoder module, feature reconstruction module, and image reconstruction module, as shown in Fig. 3.

(1) Shallow feature extraction module: 3D convolution is used to export the initial low-level features from the hyperspectral image Y, represented as $F \in \mathbb{R}^{\eta\times\lambda\times H\times W}$, where η represents the number of channels (the features after converting the original spectral data into network feature representations). This operation converts the original spectral data into feature representations suitable for deep network processing, thereby laying the foundation for subsequent feature extraction.
(2) Multi-scale encoder-decoder module: The network body consists of a five-level hierarchical structure, with each layer containing a different number of spectral spatial residual spatial-spectral recurrent transformer (SSRT) modules. This module achieves multilevel extraction of spatial spectral features through progressive downsampling and upsampling operations. Its feature propagation process can be represented as follows:

$$F^{i+1} \in R - T(F^i), i = 0, 1, \cdots, L-1, \tag{2}$$

$$F_{\text{out}} = G\big[\text{Conv}(F^L)\big] + G(F^0), \tag{3}$$

where L is the total number of SSRT blocks in each layer, set from the first to the fifth layer as [2, 2, 6, 2, 2].

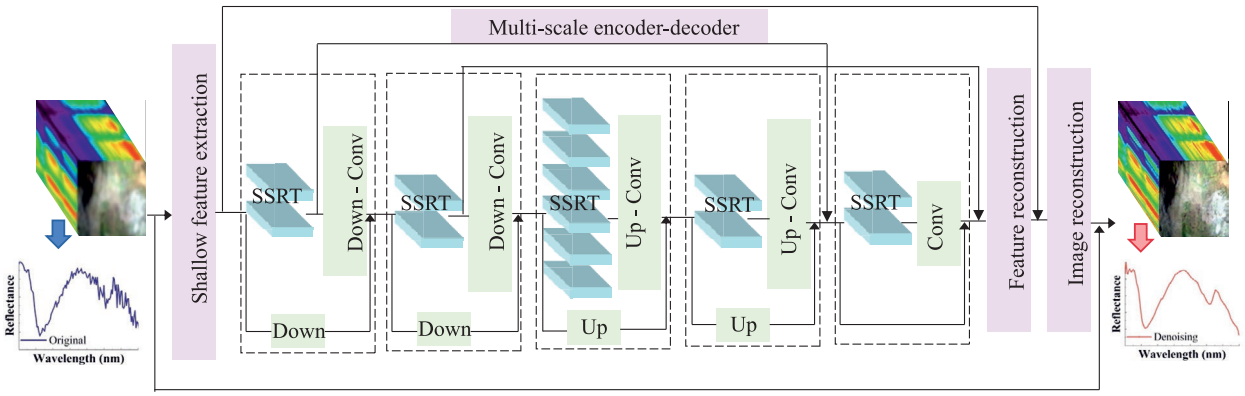

Fig. 3. Noise reduction model for hyperspectral images.

R represents the original SSRT operator. T represents the Block operator. $G(\cdot)$ represents downsampling or upsampling, and is excluded from the final decoder. The above-mentioned SSRT block is the core component of the network, innovatively integrating spectral and spatial dual-branch structures, and is used to simultaneously capture spectral correlation (inter-band relationship) and spatial self-similarity (inter-pixel relationship within a certain band).

The spectral branch treats the hyperspectral cube as a bandwise sequence. Preceding-band context is encoded by an RNN into a state representation, after which the current band is partitioned by a shift-window scheme and linearly projected onto queries, keys, and values. Cross-attention and self-attention fuse band features under the guidance of the RNN state, whereas modified simple recurrent unit (SRU) gates encode the global spectral correlation (GSC). A multi-layer perceptron (MLP) then performs feature transformation.

The spatial branch models the intraband spatial relations under GSC guidance from the spectral branch. The parameter sharing of keys/values tightly couples both branches, and self-/cross-attention updates the current band feature map. To further exploit global spectral information, the SSRT module adopts a bidirectional design that aggregates forward and backward bandwise features; combined with the shift-window strategy, it enables multi-level mining of non-local spatial self-similarity (NSS). This integration strengthens the joint spatial-spectral representation of HSI.

For each band, the forward and backward SSRT outputs are computed and fused to obtain the spatial feature map. The shift-window scheme progressively captures long-range NSS at multiple scales, thereby improving the concurrent modeling of GSC and NSS.

(3) Feature reconstruction module: After the encoder-decoder, the spatial-spectral features aggregated via 3D convolution are refined and fused with shallow features to exploit complementary hierarchies.

(4) Image reconstruction module: The fused features are upsampled and reconstructed through 3D convolutions to produce the denoised hyperspectral image.

By integrating a Transformer within an RNN framework, the spectral branch preserves the preceding-band context while learning long-range inter-band dependencies, thus exceeding the fixed-band limitations in GSC modeling. The SSRT block unifies the NSS and GSC through bidirectionality and shared key-value parameters across branches, overcoming isolated processing and enhancing spatial–spectral representation.

2.2.2 Noise reduction evaluation

To assess the robustness of the hyperspectral noise reduction methods under complex real-world conditions, experiments were conducted on spectral data acquired under four extreme imaging scenarios: low-light environments, strong illumination interference, high surface moisture, and long-distance imaging. Noise reduction performance was quantitatively evaluated using the mean peak signal-to-noise ratio (MPSNR) and structural similarity (SSIM). A block processing strategy coupled with data augmentation techniques (random flipping/cropping/scaling) was implemented to enhance model generalization.

Under photon-limited conditions, the data exhibited mixed Poisson-Gaussian noise interference with significant dark current noise, resulting in spectral curve distortion and weak signal attenuation (Chen et al., 2024). The original spectrum (blue, Fig. 4(a)) displayed non-physical negative reflectance values (minimum: –0.03, yellow box). Post-denoising (red), reflectance was restored to the physically plausible range (0.01–0.06), successfully recovering the 1900 nm water absorption feature and 2300 nm dolomite diagnostic band.

The saturation effects and optical halos induced by intense illumination caused a loss of local band information (Fig. 4(b)). The original data (blue) showed near-unity reflectance at approximately 1800 nm (orange box), indicating sensor saturation. Denoising reduced the reflectance to 0.92, while eliminating high-frequency fluctuations

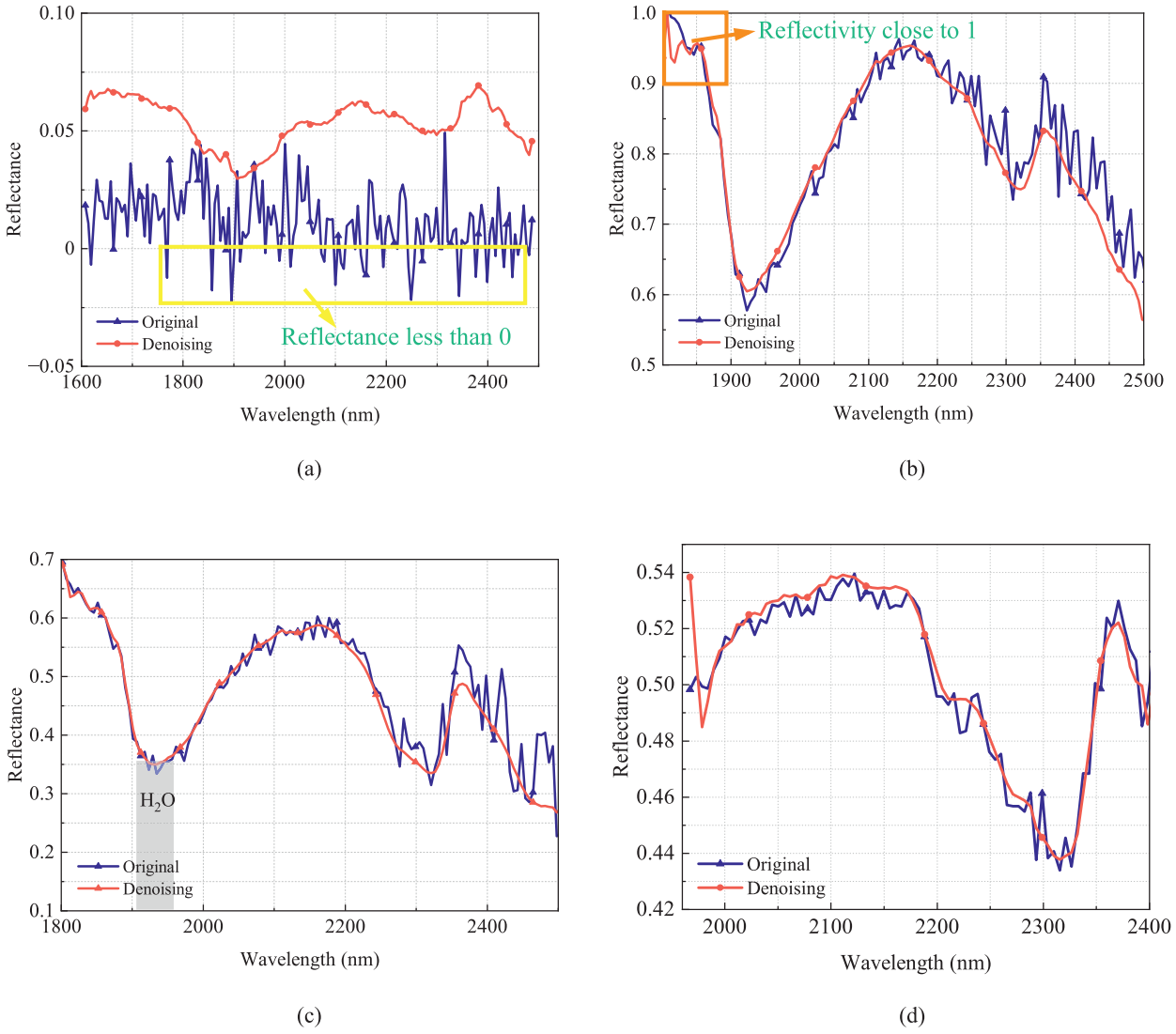

Fig. 4. Noise reduction effect under extreme imaging conditions. (a) Low light conditions, (b) interference from strong light, (c) adequate moisture, and (d) long-distance imaging.

(2050–2500 nm) attributed to thermally induced readout noise coupling. Crucially, the 2300 nm dolomite feature was preserved through joint spatial-spectral filtering.

In water-rich geotechnical engineering regions, hydrogen bonding modulates the position and width of the O–H absorption band. The original spectra exhibited anomalous reflectance fluctuations within the 1900–2100 nm water absorption band (grey zone, Fig. 4(c)), including an aberrant elevation at 1950 nm. The post-denoising absorption valleys exhibited improved symmetry and alignment with the theoretical vibrational absorption characteristics of water-bearing minerals.

In the context of long-distance imaging, the raw data displayed high-frequency noise oscillations (2090–2120 nm and 2280–2320 nm). Noise reduction applied non-local spatial constraints and spectral low-pass filtering, reducing fluctuations to ±0.005 reflectance units. Diagnostic features (e.g., 2300 nm dolomite absorption in Fig. 4(d)) maintained spectral fidelity, confirming the preservation of intrinsic material properties.

The MPSNR quantifies the fidelity of the reconstructed images, where higher values indicate a superior noise reduction performance. Let Q represent MPSNR. Q_k represents the peak signal-to-noise ratio (PSNR) of the kth band. For the denoised band image P_k and its corresponding ground-truth Z_k (both of size $H \times W$), the MPSNR is calculated as

$$Q = \frac{1}{\lambda}\sum_{k=1}^{\lambda} Q_k, \tag{4}$$

$$Q_k = 10\lg\left(\frac{V_{\mathrm{MAX}}^2}{\xi_k}\right), \tag{5}$$

$$\xi_k = \frac{1}{HW}\sum_{h}^{H}\sum_{w}^{W}(P_{h,w,k} - Z_{h,w,k})^2, \tag{6}$$

where h, w denote the spatial coordinates (pixel location) of the hyperspectral image, h represents the row index (ranging from 1 to H, where H represent the height of the hyperspectral image), w represents the column index (ranging from 1 to W, where W represent the width of the hyperspectral image), k denotes the band index (ranging from 1 to λ, where λ is the total number of bands), ξ_k represents the mean square error of the kth band, and V_{MAX} is the maximum possible pixel value.

The SSIM assesses the preservation of structural information in an image, where higher values indicate greater similarity to the reference image. Let S represent SSIM. Its calculation is defined as follows:

$$S(P,Y)=\frac{(2\mu_P\mu_Y+C_1)(2\sigma_{PY}+C_2)}{(\mu_P^2+\mu_Y^2+C_1)(\sigma_P^2+\sigma_Y^2+C_2)}, \tag{7}$$

where μ_P and μ_Y are the local means of images P and Y, respectively; σ_P^2 and σ_Y^2 are local variances; σ_{PY} is the local covariance; C_1 and C_2 are empirical constants.

The noise reduction effect on the spectral data under extreme imaging conditions is presented in Table 1. The MPSNR of the denoised image increased by 10.2952 dB compared to that of the noisy image, suggesting a significant enhancement in the overall fidelity of the pixel grayscale values. The SSIM increased from 0.6145 to 0.9195, approaching the ideal value of 1.0, demonstrating a significant improvement in the preservation of structural textures and detailed features. The quantitative results of both indicators collectively demonstrate the optimization effect of the denoising algorithm on the hyperspectral image quality, establishing a reliable data foundation for subsequent mineral spectral feature analysis.

2.3 Hyperspectral unmixing

In geological engineering exploration, hyperspectral remote-sensing technology facilitates geological information inversion by acquiring fine spectral characteristics from rocks and minerals. However, owing to constraints in sensor spatial resolution and environmental complexity, the acquired images frequently exhibit mixed-pixel effects, where a single-pixel spectral signal is composed of the spectral characteristics of multiple minerals or rock components stacked together.

2.3.1 Mixed pixel simulation

This paper presents a probabilistic mixed-pixel simulation method based on the Dirichlet distribution to address spectral mixing phenomena in tunnel engineering scenarios. The method initially randomly selects three spectral endmembers from the United States Geological Survey (USGS) standard spectral library (version s06av95a) by employing L-norm normalization preprocessing to eliminate dimensional discrepancies. Subsequently, the Dirichlet distribution is utilized to randomly generate abundance coefficients, strictly satisfying the non-negativity constraint and the sum-to-one constraint ($a_i \geq 0$, $\sum_{i=1}^{n} a_i = 1$). This method exploits the additive property of Gamma distributions: when $y_i \sim \mathrm{Gamma}(\alpha_i, 1)$ is independently and identically distributed (α_i is the shape parameter of the Gamma distribution), $S_i = \frac{y_i}{\sum y_i} \sim \mathrm{Dir}(\boldsymbol{\vartheta}), \boldsymbol{\vartheta} = (\alpha_1, \cdots, \alpha_n)$ satisfies the Dirichlet distribution. Based on this principle, the linear mixing model $\boldsymbol{r} = \sum_{i=1}^{n} a_i \boldsymbol{e}_i + \varepsilon$ (where $\boldsymbol{e}_i \in \mathbb{R}^{420\times 3}$ denotes the endmember matrix and ε is the model error) synthesizes a hyperspectral data cube with a spatial resolution of 100 × 100 pixels and 420 spectral bands covering 0.4–2.5 μm. This approach enables parametric control of the mixing degree through the convex geometry of the Dirichlet distribution, generating synthetic datasets that adhere rigorously to the physical constraints of hyperspectral unmixing while accurately replicating the spatial heterogeneity characteristics in tunnel environments.

Figure 5 illustrates the spectral characteristics of the endmembers and the corresponding abundance distribution within the virtual mixed pixels. Figure 5(a) depicts the spectral curves of three endmembers randomly selected from the USGS spectral library (simulated endmembers A, B, and C). Significant morphological variations were evident among the endmembers. This spectral differentiation facilitated the simulation of mixed pixels. Figure 5(b) presents the abundance of the three endmember types across 20 randomly selected pixels (random pixels 0–19). The endmember composition within each pixel varies randomly. For example, endmember A predominated in random pixel 0, whereas endmember B exhibited the highest abundance in random pixel 6. Thus, virtual mixed pixels featuring diverse abundance distributions effectively simulated the heterogeneous composition of mixed pixels encountered in actual scenes. Consequently, these simulations offered a varied sample set for evaluating mixed-pixel decomposition algorithms.

2.3.2 Mineral endmember extraction and content inversion

In hyperspectral data processing, mineral endmember extraction constitutes a key foundational step for achieving unmixing of mixed pixels and generating accurate mineral maps. Compared with traditional manual endmember selection, which is susceptible to subjective influence and has limited environmental adaptability in spectral library matching, the present study employs the N-FINDR algorithm for mineral endmember extraction (George et al., 2024).

N-FINDR, an algorithm grounded in convex geometry theory, operates on the principle of identifying the simplex vertex possessing the maximum volume within the data space to determine the endmembers (He et al., 2024).

Table 1
Comparison of MPSNR and SSIM between noisy images and denoised images.

Index	Noisy	Out
MPSNR	12.0115	22.3067
SSIM	0.6145	0.9195

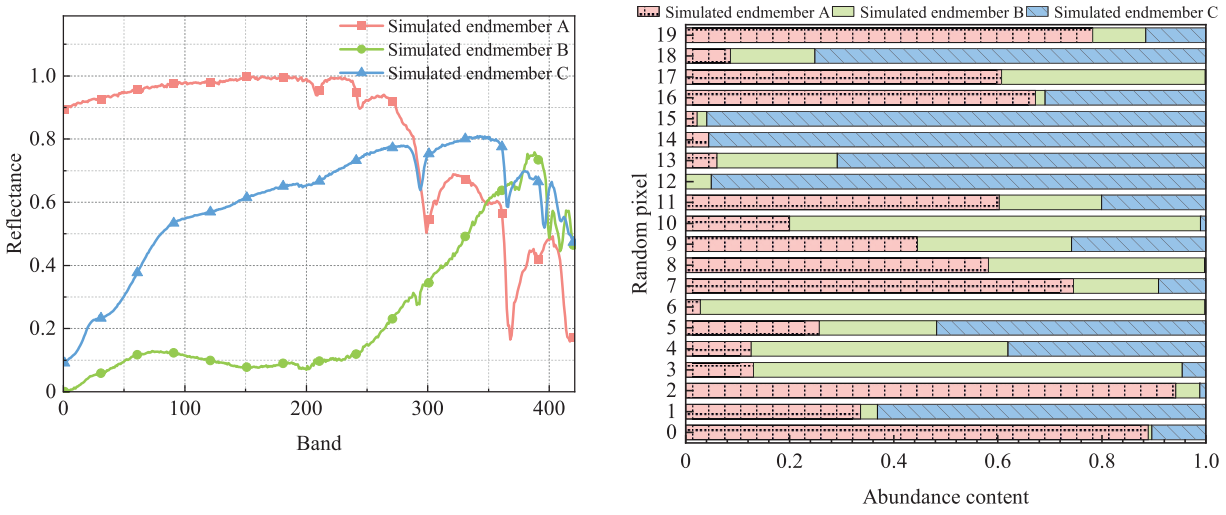

Fig. 5. Virtual mixed pixel end elements and abundance information. (a) USGS random endmember, and (b) random pixel endmember abundance.

Within the spectral feature space of the hyperspectral data, all pixel spectral vectors collectively form a convex geometry, wherein the spectra of pure mineral endmembers correspond to the vertices of this convex geometry. The endmember set $\{\boldsymbol{e}_1, \boldsymbol{e}_2, \cdots, \boldsymbol{e}_p\}$ is determined such that $\max V(\boldsymbol{e}_1, \boldsymbol{e}_2, \cdots, \boldsymbol{e}_p)$. The combination of vertices of a single body with the largest volume represents the purest endmember. For the p end elements (corresponding to the $p-1$ dimensional space), the simple volume V formed is

$$V = \frac{1}{(p-1)!}\left|\det[\boldsymbol{e}_1 - \boldsymbol{e}_p, \boldsymbol{e}_2 - \boldsymbol{e}_p, \cdots, \boldsymbol{e}_{p-1} - \boldsymbol{e}_p]\right|, \tag{8}$$

where det is the determinant value (the absolute value of the determinant reflects the "hypervolume" of the monomer in $p-1$ dimensional space), and $\boldsymbol{e}_1, \boldsymbol{e}_2, \cdots, \boldsymbol{e}_p$ is the endmember spectral vector.

The calculation process is as follows, as shown in Fig. 6.

(1) Initialization: p pixels are randomly selected from the hyperspectral dataset as initial endmembers $\boldsymbol{E}^{(0)} = \left\{\boldsymbol{e}_1^{(0)}, \cdots, \boldsymbol{e}_p^{(0)}\right\}$ to form a simplex, with its vertices being the selected pixels. Based on the above volume formula, the current volume V_{current} of the simplex is calculated.

(2) Replacement test: For each pixel $X_t \in \mathbb{R}^{p-1}$ after dimensionality reduction (covering all pixel samples in hyperspectral data), each endmember $\boldsymbol{e}_j$ in the current endmember set is sequentially replaced to generate a temporary endmember set $\boldsymbol{E}^j$, and the corresponding simplex volume V_{new}^j is calculated.

(3) Update: If there exists a candidate pixel j such that $V_{\text{new}}^j > V_{\text{current}}$, then the X_t that maximizes the simplex volume is selected to replace the corresponding endmember $\boldsymbol{e}_j$, and the set of endmembers E is updated.

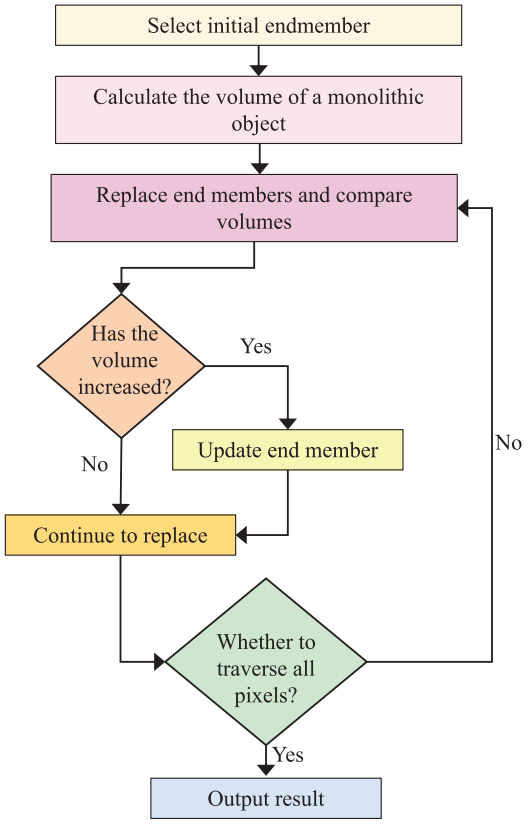

Fig. 6. Schematic diagram of N-FINDR algorithm flow.

(4) To avoid convergence to local optima, the algorithm employs random initialization and multiple iterations. When the simplex volume no longer increases or the maximum iteration count is reached, the algorithm terminates and outputs the optimal endmember set.

This study was based on the principle of mineral reflectance spectroscopy, which posits that mixed spectra represent linear combinations of the constituent mineral spectra. The validity of this assumption arises from its adherence to the Beer–Lambert law. Under ideal conditions, this principle establishes that the spectral response exhibited by mixed pixels comprising multiple mineral components constitutes a weighted superposition of the pure mineral spectra proportional to their relative abundances. The FCLS method, which implements the linear mixed model, incorporates two strict physical constraints: the non-negativity of abundances and the sum-to-one constraint. These constraints facilitate the optimal estimation of endmember abundance within mixed pixels (Ducasse et al., 2024), thus enabling mineral mapping. In this model, the spectrum of a mixed pixel is formulated as a linear combination of the endmember spectra:

$$\begin{aligned} \boldsymbol{r} &= \sum_{i=1}^{n} a_i \boldsymbol{e}_i + \varepsilon \\ & a_i \geq 0 \quad , \\ & \sum_{i=1}^{n} a_i = 1 \end{aligned} \tag{9}$$

where $\boldsymbol{r}$ is the mixed pixel spectral vector, which represents the raw spectral data collected by the hyperspectral sensor; a_i is the abundance of the ith endmember, which characterizes the relative content of the corresponding mineral in the mixed pixel; $\boldsymbol{e}_i$ is the spectral vector of the ith endmember, which represents the spectral characteristics of pure minerals; ε is the model error, which is used to characterize spectral residuals that cannot be explained by linear models, including interference factors such as sensor noise and nonlinear mixing effects.

In practical applications, the FCLS method imposes dual physical constraints on linear mixing models. First, the non-negativity constraint ensures that mineral abundances conform to physical reality, eliminating physically implausible negative values. Second, the sum-to-one constraint reflects the conservation of mass, which requires all mineral abundances to sum to unity. By constructing a constrained objective function and solving it using Lagrange multipliers or quadratic programming, FCLS minimizes the spectral reconstruction error while preserving the physical validity of the unmixing results. Consequently, the unmixed endmember abundances were mapped as spatial distributions.

2.3.3 Spectral reconstruction and quantitative inversion evaluation

To verify the reliability of the endmember extraction and mixed decomposition, this study reconstructed the original hyperspectral data based on a linear mixed model and quantified the inversion accuracy using the RMSE and spectral angle mapper (SAM).

In the process of spectral reconstruction, for each pixel (spatial position (h, w)), the reconstructed reflectance $\hat{\boldsymbol{r}}_p$ is generated by a linear combination of the endmember matrix $\boldsymbol{E} \in \mathbb{R}^{\lambda \times \beta}$ (λ is the total number of spectral bands and β is the number of endmembers) and the abundance vector $\boldsymbol{a}_i \in \mathbb{R}^{\beta}$, satisfying $\hat{\boldsymbol{r}}_p = \boldsymbol{E} \cdot \boldsymbol{a}_i$. The abundance vector was solved using nonnegative least squares optimization.

The RMSE is used to evaluate the reflectance error between the original and reconstructed spectra, and its calculation formula is as follows:

$$\gamma = \sqrt{\frac{1}{\lambda} \sum_{z=1}^{\lambda} (O_z - R_z)^2}, \tag{10}$$

where γ represents RMSE, O_z is the reflectance of the original spectrum in the zth band, R_z is the reflectance of the reconstructed spectrum in the zth band, and B is the total number of bands in the spectrum.

SAM evaluates the fidelity of a spectral shape by calculating the angle between the spectral vectors of each pixel and the reconstructed vector. The lower the value, the more similar the spectrum. For the pixel point (h, w), the spectral vector of the original image (with height × width dimensions of $H \times W$) is $\boldsymbol{\chi}$, and the spectral vector of the reconstructed image is $\boldsymbol{\beta}$, with a spectral angle of $\theta = \arccos\left(\frac{\boldsymbol{\chi} \cdot \boldsymbol{\beta}}{\|\boldsymbol{\chi}\| \|\boldsymbol{\beta}\|}\right)$. The mean spectral angle of all the pixels is.

$$v = \frac{1}{HW} \sum_{h=1}^{H} \sum_{w=1}^{W} \theta_{h,w}, \tag{11}$$

where v represents SAM.

The quantitative inversion accuracy of the virtual hyperspectral images was evaluated using RMSE and SAM. The overall RMSE was 0.2540 and the SAM was 0.4327 rad, indicating acceptable inversion performance. For five randomly sampled pixels, the RMSE values ranged from 0.2402 to 0.2771, with the lowest at (5, 30) and the highest at (76, 13), which was likely due to the greater spectral mixing complexity. The original spectral means ranged from 0.5517 to 0.5690, and the deviations between the reconstructed and original means were consistently <0.01, demonstrating the effective preservation of the spectral energy distribution. The SAM values ranged from 0.4000 to 0.4769 rad, with pixel (5, 30) exhibiting the smallest SAM (0.4000 rad), reflecting the highest spectral shape similarity (Table 2). Overall, both metrics confirm that the inversion model achieves stable accuracy and maintains the spectral energy characteristics in the virtual dataset.

2.4 Verification

Rock samples collected in situ from a tunnel engineering site were analyzed using an indoor hyperspectral imaging system (Fig. 7(a)). This system incorporates an imaging hyperspectral spectrometer operating in the 1000–2500 nm spectral range, utilizing a 300 W tungsten halogen lamp light source with an image acquisition working

Table 2
Quantitative inversion accuracy evaluation of virtual hyperspectral images.

Evaluation Sample	RMSE	SAM (rad)	Original spectral mean	Reconstruct spectral mean
Virtual hyperspectral	0.2540	0.4327	–	–
Random pixel (76, 13)	0.2771	0.4769	0.5530	0.5524
Random pixel (0, 89)	0.2502	0.4273	0.5600	0.5518
Random pixel (58, 14)	0.2664	0.4588	0.5517	0.5521
Random pixel (37, 65)	0.2648	0.4498	0.5612	0.5519
Random pixel (5, 30)	0.2402	0.4000	0.5690	0.5525

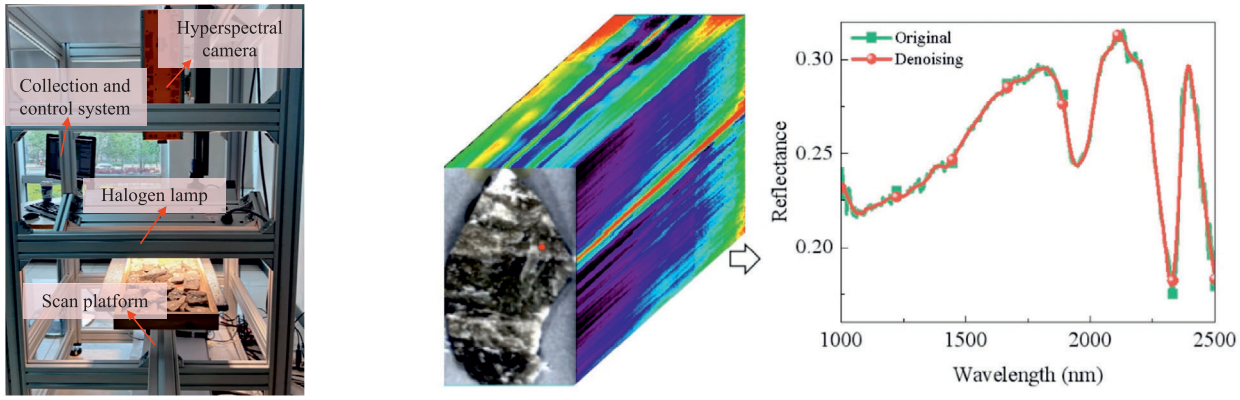

(a) (b)

Fig. 7. Indoor hyperspectral image acquisition and noise reduction. (a) Indoor hyperspectral image acquisition system (Xu et al., 2025a), and (b) spectral noise reduction effect.

distance of 70 cm. The raw hyperspectral image data exhibited a spectral resolution of 12 nm.

The hyperspectral noise reduction method proposed in this study was applied to process indoor hyperspectral images. The denoised spectral curves became smoother, suppressing noise while maintaining key spectral features such as absorption and reflection peaks (Fig. 7(b)). This confirms that the noise reduction method effectively improves the hyperspectral data quality by removing Gaussian noise, pulse noise, and stripe noise. The resulting data accurately preserves spectral information and spatial details, enabling reliable mineral identification and compositional analysis.

Mineral identification was conducted using denoised hyperspectral images of the tunnel wall rock. Mixed-pixel unmixing revealed two phases: dolomite and calcite. Figure 8 shows their spatial abundance, with red areas indicating higher content. Limestone recognition relies on asymmetric absorption in the 2300–2400 nm range, marked by a broad left flank and a narrow right flank, enabling clear discrimination from other minerals. Cation composition differences yield distinct spectral signatures (Fig. 8(c)): dolomite ($CaMg(CO_3)_2$) has a strong absorption at 2320 nm, while calcite ($CaCO_3$) peaks near 2340 nm.

To obtain quantitative mineral composition data, XRD analysis was conducted on samples from representative points. The collected samples were pulverized, pelletized, and subjected to XRD testing. These results provide a reference validation for imaging spectroscopy analysis. The partial XRD results presented in Fig. 9 confirm that the sample was predominantly composed of calcite and accessory dolomite.

3 Engineering application

3.1 In situ acquisition and noise reduction of tunnel hyperspectral

To assess the feasibility of hyperspectral imaging technology in tunnel environments and the efficacy of in situ large-scale rock and mineral analysis methods at engineering sites, this study was conducted within a water diversion tunnel in Shanxi, China. The tunnel site traverses the Upper Cambrian Gushan Formation (∈3g), exhibiting a gatemouth-shaped cross-section. The host rock primarily comprises limestone.

Given that the principal spectral response characteristics of minerals occur within the 2000–2400 nm range, spectral dimensionality reduction was applied to the original spectra to mitigate the computational complexity, as detailed in Table 3.

Figure 10 presents a comparison of the original and denoised spectral curves (2200–2400 nm key mineral diagnostic bands) for three randomly selected points in each of

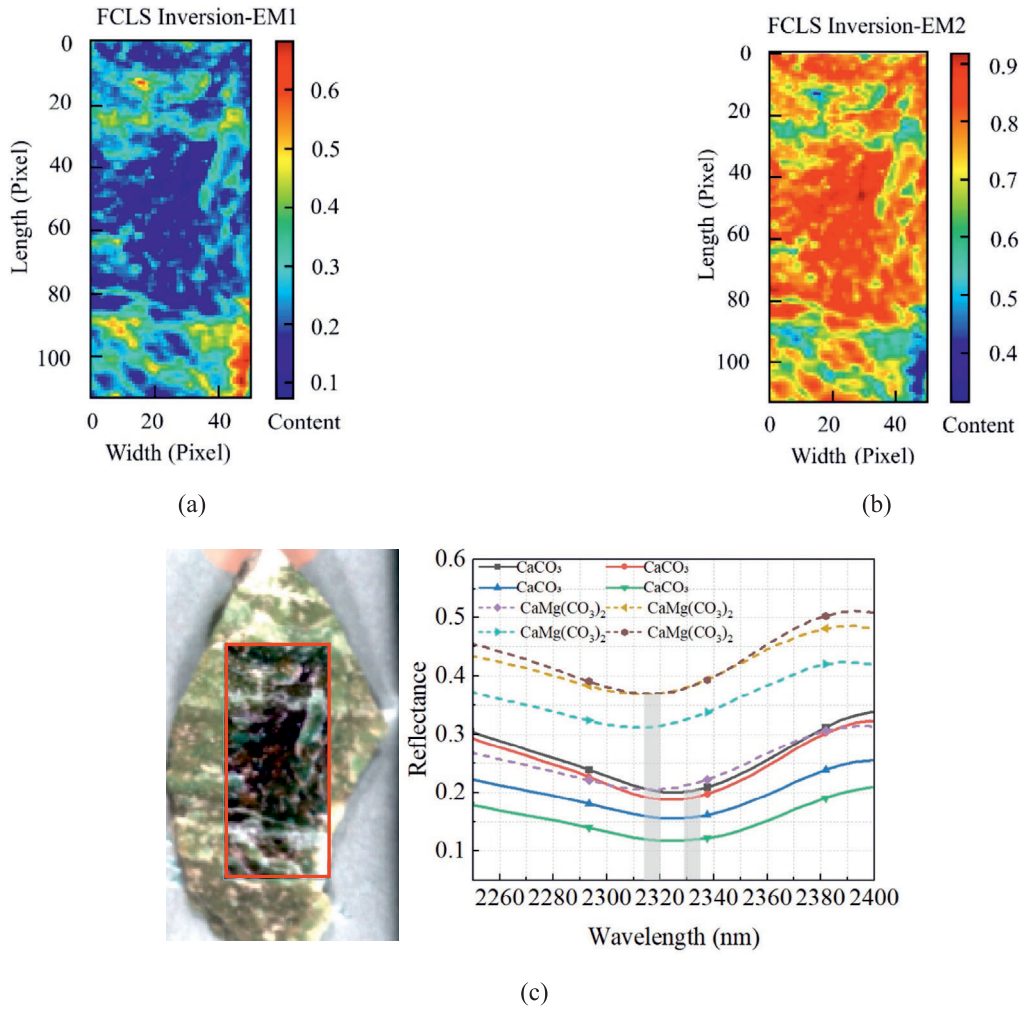

Fig. 8. Indoor rock and mineral hyperspectral analysis. (a) Distribution map of dolomite content, (b) distribution map of calcite content, and (c) spectral curve.

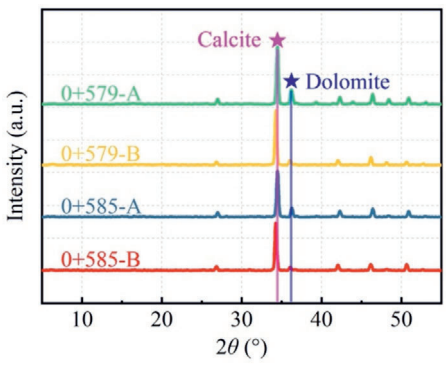

Fig. 9. XRD test results.

the four typical tunnel areas. Figure 10(a1)–(a3) illustrates the original and denoised spectral reflectance for locations (89, 259), (138, 516), and (191, 126) in water diversion tunnel area I. The original spectrum at location (138, 516) exhibits irregular fluctuations within the 2050–2150 nm range, whereas the denoised curve exhibits greater smoothness while retaining critical absorption features. Similarly, Fig. 10(b1)–(b3) depicts the comparison for area II. The original spectra from locations (203, 317) and (241, 626) display high-frequency noise between 2100 and 2200 nm; noise reduction attenuated this noise but also removed some diagnostic spectral features. The noise reduction outcomes for areas III (Fig. 10(c1)–(c3)) and IV (Fig. 10(d1)–

Table 3
In situ hyperspectral images of tunnels.

Evaluation object	After processing–wavelength range (nm)	Wave number	Size (height × width)
Water diversion tunnel area I	2003–2395	42	906 × 384
Water diversion tunnel area II	2003–2395	42	910 × 384
Water diversion tunnel area III	2252–2395	16	873 × 384
Water diversion tunnel area IV	2089–2376	31	896 × 384

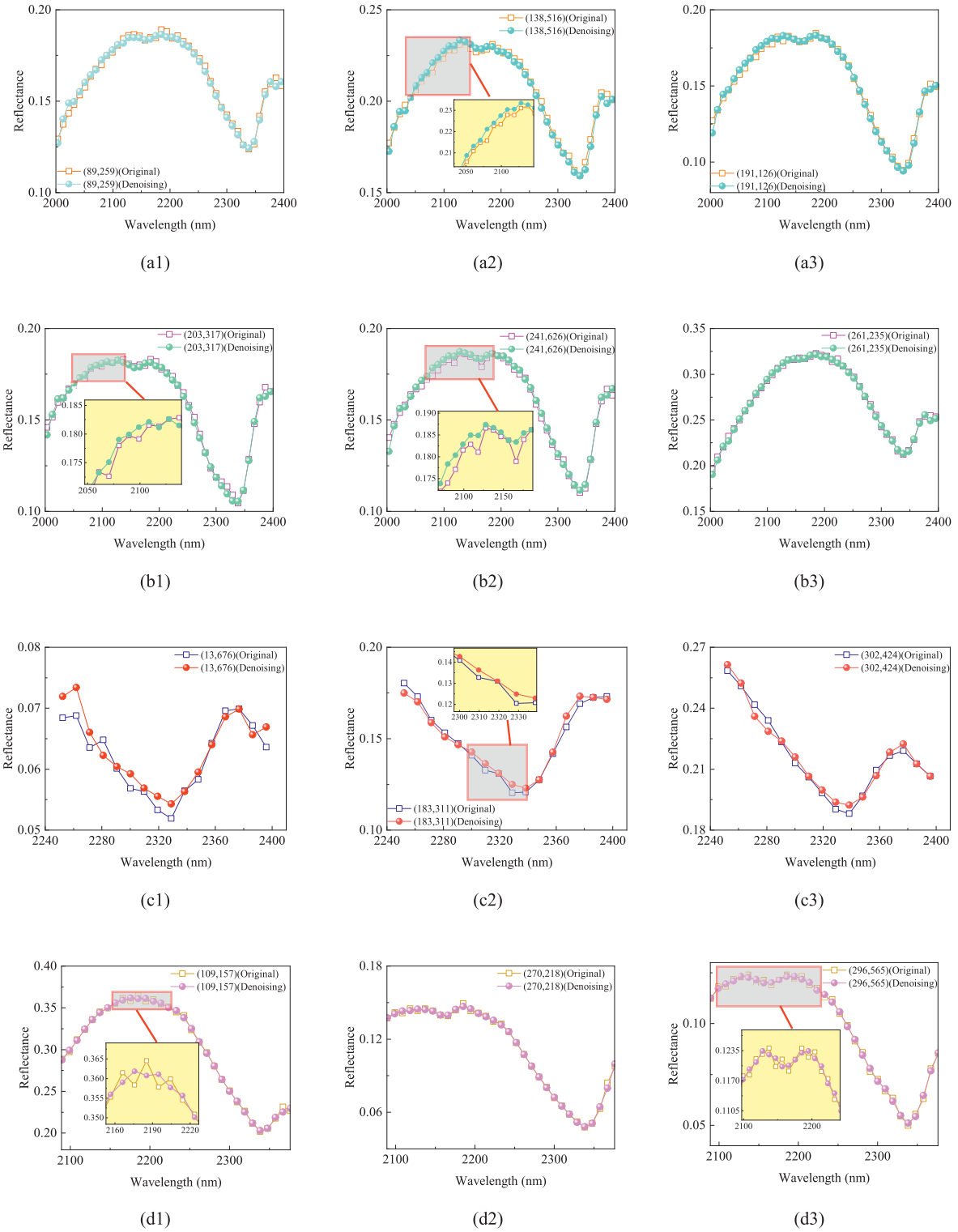

Fig. 10. Noise reduction effect of hyperspectral images. (a1) Water diversion tunnel area I location (89, 259), (a2) water diversion tunnel area I location (138, 516), (a3) water diversion tunnel area I location (191, 126), (b1) water diversion tunnel area II location (203, 317), (b2) water diversion tunnel area II location (241, 626), (b3) water diversion tunnel area II location (261, 235), (c1) water diversion tunnel area III location (13, 676), (c2) water diversion tunnel area III location (183, 311), (c3) water diversion tunnel area III location (302, 424), (d1) water diversion tunnel area IV location (109, 157), (d2) water diversion tunnel area IV location (270, 218), and (d3) water diversion tunnel area IV location (296, 565).

(d3)) demonstrate comparable noise reduction characteristics. These findings substantiate that the proposed method effectively preserves diagnostic spectral fingerprints of rocks and minerals (e.g., absorption features associated with functional groups such as Al-OH and CO_3^{2-}) while suppressing random noise.

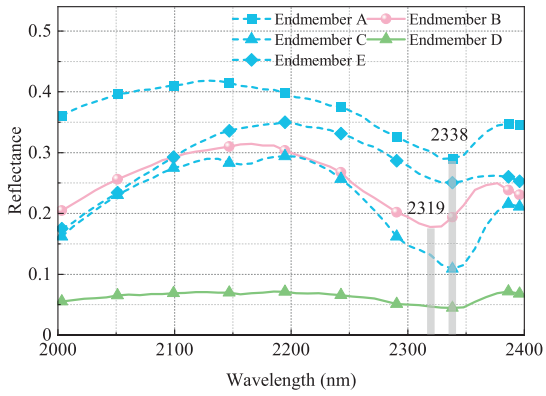

(a1)

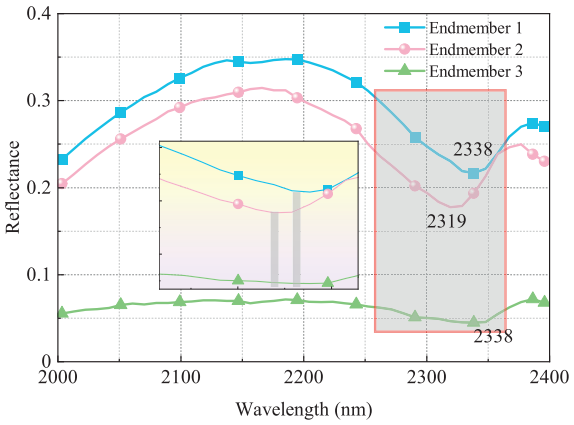

(a2)

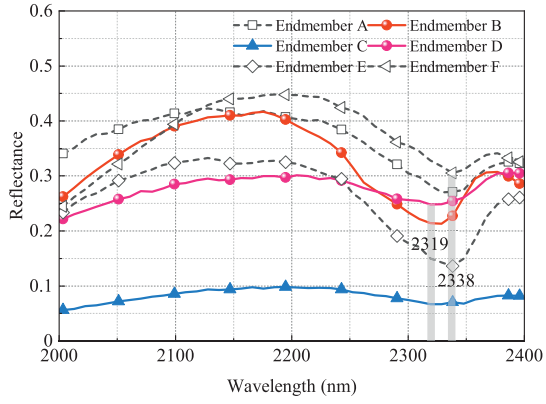

(b1)

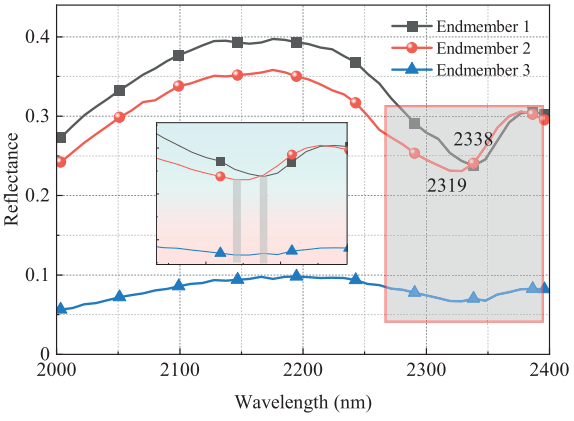

(b2)

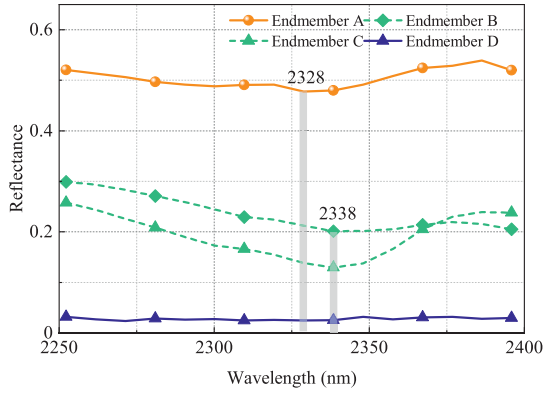

(c1)

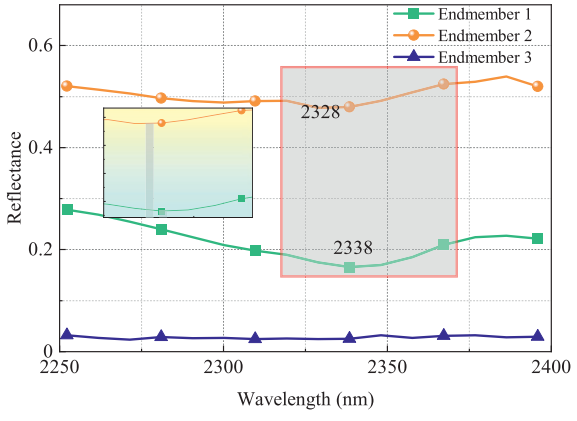

(c2)

Fig. 11. Endmember extraction in different regions. (a1) Endmember spectra of water diversion tunnel area I, (a2) endmember spectral merging of water diversion tunnel area I, (b1) endmember spectra of water diversion tunnel area II, (b2) endmember spectral merging of water diversion tunnel area II, (c1) endmember spectra of water diversion tunnel area III, (c2) endmember spectral merging of water diversion tunnel area III, (d1) endmember spectra of water diversion tunnel area IV, and (d2) endmember spectral merging of water diversion tunnel area IV.

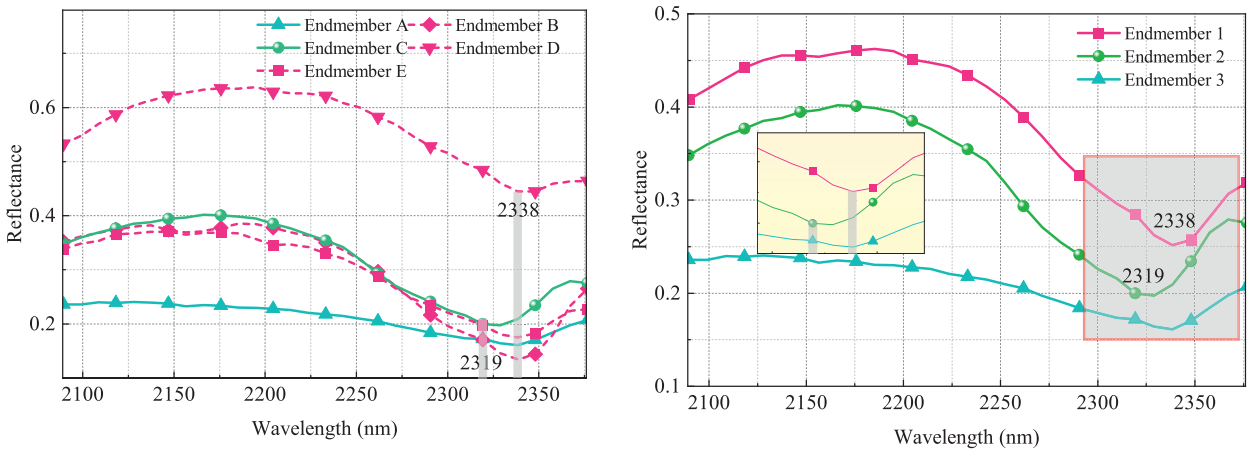

Fig 11. *(continued)*

3.2 Extraction of endmember minerals from wall rock

Utilizing the N-FINDR algorithm, five independent endmember spectra were extracted from water diversion tunnel area I, as presented in Fig. 11(a1). These spectra spanned the short-wave infrared (SWIR) band from 2003 to 2395 nm, exhibiting significant spectral divergence at the diagnostic wavelengths of 2319 and 2338 nm. Endmembers A, C, and E displayed the characteristic absorption features of calcite minerals at 2338 nm (reflectance >0.1) with analogous spectral morphologies (McCormick et al., 2021). Consequently, they were consolidated into endmember 1 during spectral optimization, as shown in Fig. 11(a2). Endmember B demonstrated a distinct absorption feature at 2319 nm, indicative of dolomite (Kurz et al., 2022). Endmember D exhibited a uniformly low reflectance (<0.1) with minimal absorption at 2338 nm. Following spectral merging and refinement (Fig. 11(a2)), the five initial endmembers were optimized to three core endmembers exhibiting diagnostic features at 2338 nm (endmember 1), 2319 nm (endmember 2), and 2338 nm (endmember 3). The reflectance of endmember 1 exceeded 0.2, whereas that of endmember 3 remained below 0.1, across the full spectral range.

In area II, six endmember spectra were extracted via the N-FINDR algorithm (Fig. 11(b1)), covering 2003–2395 nm. Pronounced spectral variations were observed at 2319 and 2338 nm. Endmembers A, E, and F showed calcite-specific absorption at 2338 nm (reflectance >0.1) with similar profiles and were merged as endmember 1 (Fig. 11(b2)). Endmembers B and D shared absorption at 2319 nm and were merged as endmember 2. Endmember C had a consistently low reflectance (<0.1) with negligible absorption at 2338 nm. After optimization, the six endmembers were reduced to three with diagnostic features at 2338, 2319, and 2338 nm. The reflectance of endmember 1 exceeded 0.2, while that of endmember 3 remained below 0.1.

In area III, four endmember spectra were obtained (Fig. 11(c1)), spanning 2252–2395 nm. Distinct features appear at 2328 and 2338 nm. Endmembers B and C, both with calcite absorption at 2338 nm (reflectance >0.1), were merged as endmember 1 (Fig. 11(c2)). Endmember A showed dolomite-specific absorption at 2328 nm, and endmember D had a uniformly low reflectance (<0.1) with minimal absorption at 2338 nm. The optimization yielded three endmembers with absorptions at 2338 nm (endmember 1), 2328 nm (endmember 2), and 2338 nm (endmember 3). The reflectance of endmember 1 exceeded 0.2, whereas that of endmember 3 remained below 0.1, likely due to illumination effects.

In area IV, five endmember spectra were extracted (Fig. 11(d1)), covering 2089–2376 nm. Significant variations were observed at 2319 and 2338 nm. Endmembers B, D, and F, all with calcite absorption at 2338 nm (reflectance >0.1), were merged as endmember 1 (Fig. 11(d2)). Endmember C exhibited dolomite absorption at 2319 nm, and endmember A showed minimal variation with negligible absorption at 2338 nm. Optimization reduced the five endmembers to three, with diagnostic features at 2338, 2319, and 2338 nm. The reflectance of endmember 1 exceeded 0.25, whereas that of endmember 3 remained below 0.25.

3.3 Quantitative inversion and mapping of wall rock minerals

Figure 12 presents the mineral abundance distribution maps derived from the FCLS inversion for different regions of the water diversion tunnel. Each subfigure employs a uniform pseudo-color scheme (range: 0–1) to represent mineral abundance, with red and blue indicating high- and low-abundance zones, respectively. Figure 12(a) depicts the abundance distributions of the calcite I, dolomite, and calcite II endmembers in tunnel area I. As illustrated in Fig. 12(b), dolomite exhibits a zonal distribution pattern with localized edge dissolution textures, potentially associated with hydrothermal channel influence.

3.4 Evaluation of inversion accuracy

To verify the reliability of the endmember extraction and mixed decomposition, we reconstructed the original hyperspectral data based on a linear mixed model and quantified the inversion accuracy using both RMSE and SAM metrics. The experimental results (Table 4) indicate that the RMSE of the diversion tunnel areas I, II, and III was as low as 0.009 500, 0.011 858, and 0.006 600, respectively. The mean SAM values were 0.0409, 0.0449, and 0.0539 rad, respectively, verifying the effectiveness of the linear mixed model and endmember spectral library

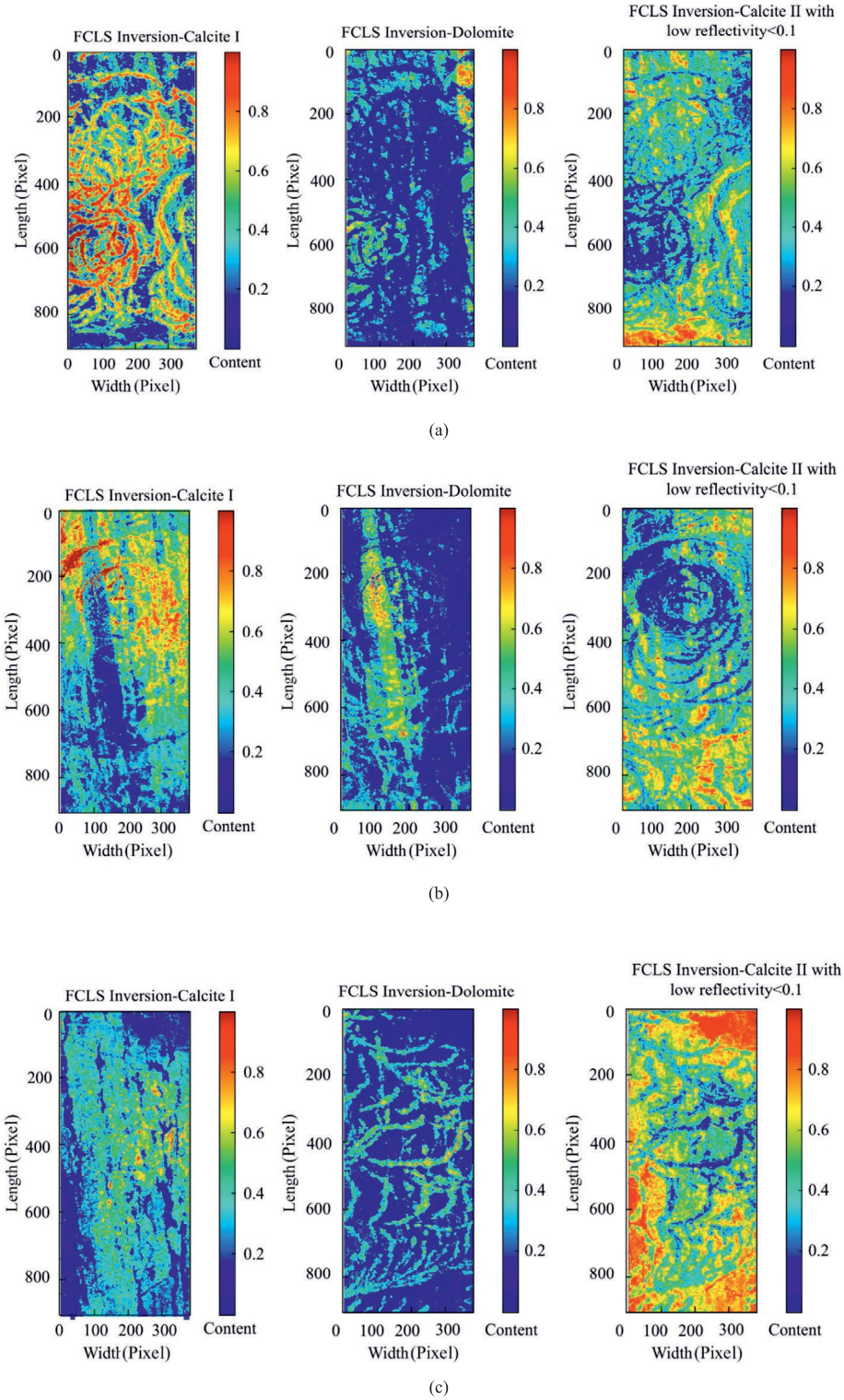

Fig. 12. Results of spatial distribution inversion of mineral abundance. (a) Water diversion tunnel area I, (b) water diversion tunnel area II, (c) water diversion tunnel area III, and (d) water diversion tunnel area IV.

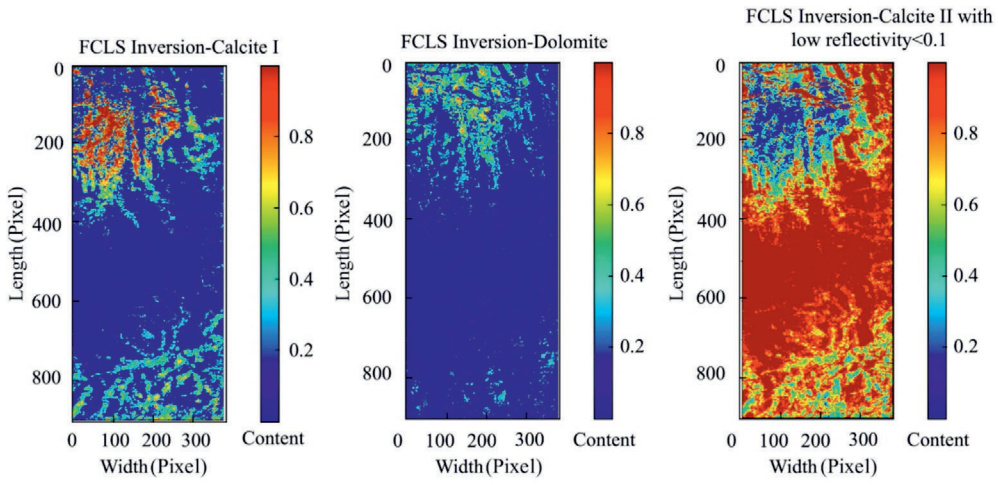

(d)

Fig 12. *(continued)*

in homogeneous terrain scenes. In area IV, the RMSE and SAM values increased to 0.052 600 and 0.0859 rad, respectively, indicating a certain accuracy gap in the complex mixed region.

Figure 13 compares the spectral reconstructions of random pixels across different regions. In area I, pixel (109, 161) shows a reflectance deviation <0.05, at bands 35–40, whereas pixel (880, 216) has a maximum deviation of 0.016 at bands 30–40. The spectra of the pixel (786, 110) almost completely overlapped (Fig. 13(a1)–(a3)). In area II, pixel (250, 349) exhibits high-frequency oscillations, with a reflectance shift at bands 30–35 that increased the SAM, likely due to shadow-induced bias in endmember abundance estimation. Pixel (829, 355) shows a deviation <0.007 at bands 10–26, and pixel (822 299) exhibits near-complete spectral consistency (Fig. 13(b1)–(b3)). In area III, pixels (633, 252), (601, 215), and (691, 200) display minimal deviations across all wavelengths, indicating effective unmixing (Fig. 13(c1)–(c3)). In area IV, the three sampled pixels show noticeable spectral shifts, but the positions of the diagnostic troughs remain unchanged (Fig. 13(d1)–(d3)).

4 Discussion

This study presents an innovative hyperspectral imaging methodology for the remote sensing detection of geological conditions in underground tunnel environments. To address extreme low-light, non-uniform radiation, and dust interference in tunnels, this study integrates SSRT denoising into hyperspectral image processing. Compared with conventional methods that overlook hyperspectral cube geometry (Bodrito et al., 2021; Chang et al., 2017), rely on local convolution or low-rank priors (He et al., 2020), and ignore long-range spatial-spectral correlations (Xiong et al., 2022), the proposed approach suppresses multi-source mixed noise, preserves diagnostic mineral spectral features, and improves long-distance imaging, providing a robust basis for high-precision mineral inversion in complex geology. Building on mixed-pixel decomposition theory, an in situ semi-quantitative inversion model was developed to overcome the subjectivity and off-site limitations of visual geological identification (a comparison of various methods is provided in Table 5) (Xu et al., 2025a) and advance beyond the qualitative spectral-library matching methods commonly used in prior work (Akgül & Ural, 2024; Govil et al., 2018; Okada et al., 2020).

Table 4
Evaluation of inversion accuracy of spectral reconstruction in different regions.

Evaluation object	RMSE	SAM (rad)
Water diversion tunnel area I	0.009 500	0.0409
Water diversion tunnel area II	0.011858	0.0449
Water diversion tunnel area III	0.006 600	0.0539
Water diversion tunnel area IV	0.052 600	0.0859

Under static illumination, multi-angle light superposition causes (i) specular reflection from non-Lambertian surfaces, producing coexisting overexposure and shadows (Fig. 14(a)), and (ii) radiance heterogeneity from the surface roughness, with overlapping illumination and edge shadows (Fig. 14(b)) (Meng et al., 2024). Hyperspectral denoising mitigates these effects but fails in ultralow-reflectance areas, highlighting the need for improved acquisition. Future directions include a line-scan narrowband source synchronized with push-broom imaging, band-matching to mineral absorption peaks (e.g., Fe^{3+} at 650 nm, Al-OH at 2200 nm), polarization modulation to suppress reflections, and thermal-radiation correction (Jia et al., 2019). Inertial compensation and compact layouts are recommended for confined spaces.

A tunnel-specific radiation transfer model that incorporates rock roughness, incidence angle, and dust scattering is required to support denoising and inversion. Based on the

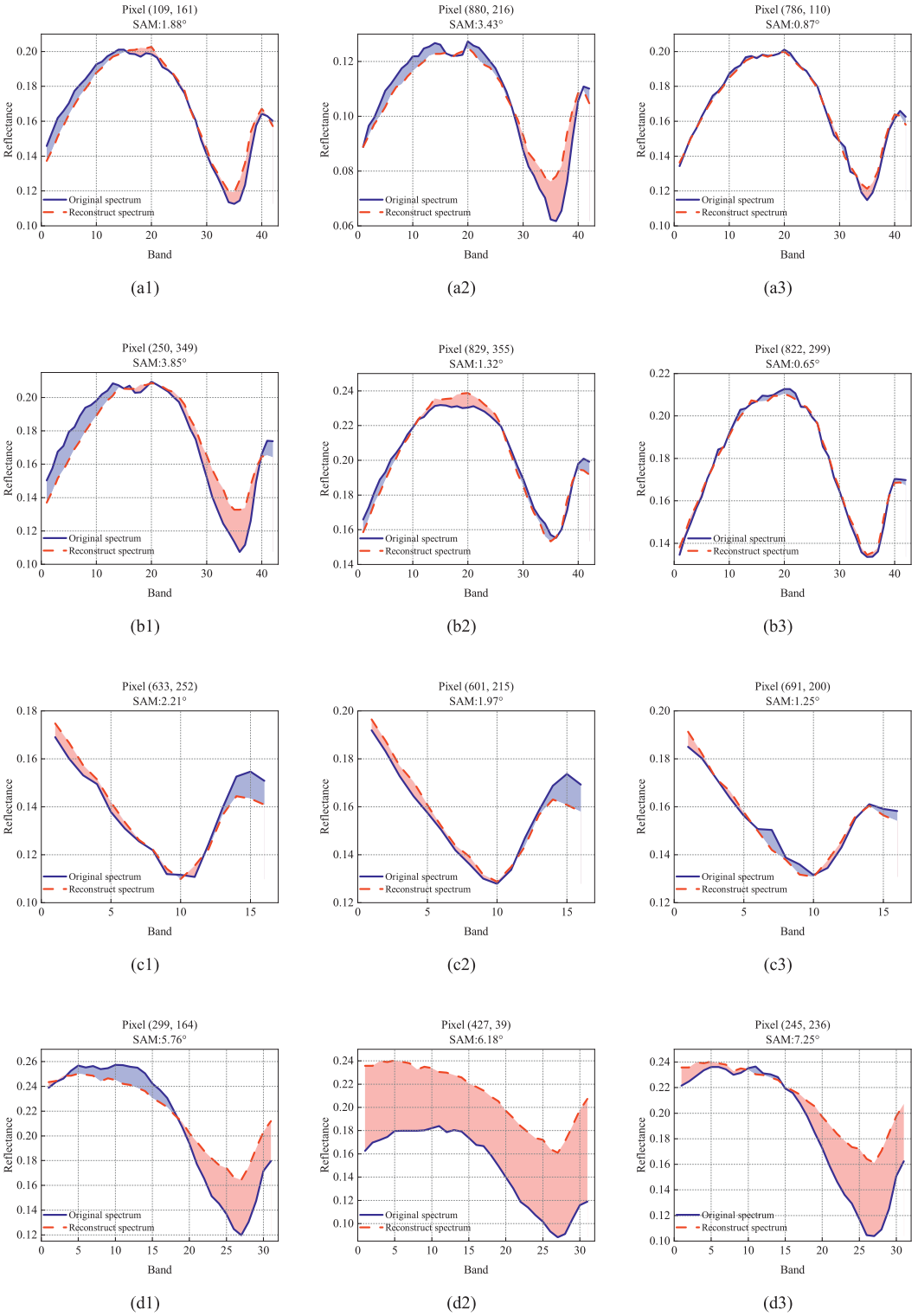

Fig. 13. Spectral differences between random points in different regions and locations. (a1) Water diversion tunnel area I random point (109, 161), (a2) water diversion tunnel area I random point (880, 216), (a3) water diversion tunnel area I random point (786, 110), (b1) water diversion tunnel area II random point (250, 349), (b2) water diversion tunnel area II random point (829, 355), (b3) water diversion tunnel area II random point (822, 299), (c1) water diversion tunnel area III random point (633, 252), (c2) water diversion tunnel area III random point (601, 215), (c3) water diversion tunnel area III random point (691, 200), (d1) water diversion tunnel area IV random point (299, 164), (d2) water diversion tunnel area IV random point (427, 39), and (d3) water diversion tunnel area IV random point (245, 236).

Table 5
Comparison of this method with traditional mineral identification methods.

Comparison dimension	Macroscopic geological identification (visual observation)	Laboratory analysis (XRD, microscopic analysis)	Hyperspectral imaging technology (this study)
Detection mode	Field identification relying on human experience	Sample collection followed by laboratory analysis	In situ, non-destructive testing
Analysis efficiency	Highly influenced by subjective experience	Single sample preparation (grinding/thin sectioning), total analysis time ≥20 min	Single scan covering 1 m^2 takes ≥5 min
Quantitative capability	Only qualitative description possible, cannot be quantified	Quantitative analysis possible, dependent on standard sample fitting	Based on pixel decomposition, outputs mineral abundance (0–1 quantitative values)
Spatial information	Limited spatial information with low accuracy and high subjectivity	Single-point or single-sample analysis; discrete data lacking spatial continuity	Area-based imaging directly producing two-dimensional maps of mineral type and abundance
Engineering adaptability	Limited applicability; feasible during construction breaks but relies entirely on manual judgement	Poor adaptability; necessitates construction interruption for sampling; laboratory workflow incompatible with rapid excavation	High adaptability; enables in situ rapid detection compatible with the "excavate-and-test-simultaneously" requirements of tunnel construction

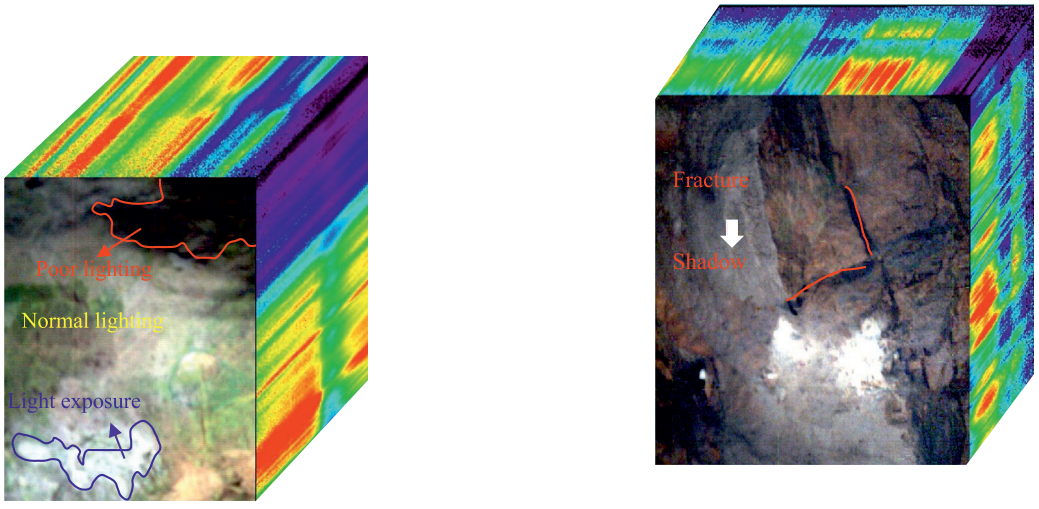

(a) (b)

Fig. 14. Challenges of in situ acquisition of hyperspectral images in tunnels. (a) Uneven illumination, and (b) uneven surface.

abundance results, a mineral–fracture–mechanical parameter linkage model can further extend hyperspectral applications to rock mechanics assessments.

5 Conclusions

In this study, in situ tunnel detection was implemented using subsurface imaging hyperspectral technology to establish a novel method for mineral mapping in tunnels. The main conclusions are as follows.

(1) To address hyperspectral image degradation from challenging tunnel conditions (low illumination and dust interference), we introduced an integrated SSRT within the U-Net architecture. This framework effectively captures crossband spectral correlations and nonlocal spatial dependencies, significantly enhancing the signal-to-noise ratio and spectral fidelity of denoised tunnel hyperspectral imagery.
(2) A Dirichlet distribution-based mixed-pixel simulation approach was developed to replicate the spectral mixing phenomenon in tunnels. The generated virtual spectra with diverse abundance distributions provided realistic samples for validating spectral unmixing algorithms under complex compositional scenarios.
(3) Endmember minerals were extracted using the N-FINDR algorithm to identify the spectrally pure pixels and clarify the diagnostic absorption features at the tunnel faces. Subsequent FCLS inversion quantified the wall-rock mineral abundances, enabling the rapid identification of mineral assemblages. The spec-

tral reconstruction validation, as quantified by RMSE and SAM, confirmed the reliability and accuracy of the unmixing methodology.

(4) When applied to a Shanxi water diversion tunnel, this approach successfully identified dolomite and calcite distributions while quantifying the regional mineral contents. Compared with conventional macroscopic identification, it enables a paradigm shift from qualitative analysis to semi-quantitative/quantitative in situ detection. Relative to laboratory-based methods, the in situ noncontact approach reduces the analysis time while providing large-area coverage, significantly accelerating construction safety and efficiency.

Data availability

The data that support the findings of this study are available from the corresponding author upon reasonable request.

CRediT authorship contribution statement

Shan Li: Writing – original draft, Visualization, Formal analysis, Data curation. **Peng Lin:** Writing – review & editing, Validation, Funding acquisition. **Kai Yang:** Validation, Investigation. **Zhenhao Xu:** Validation, Supervision, Methodology, Funding acquisition, Conceptualization.

Declaration of competing interest

The authors declare that they have no known competing financial interests or personal relationships that could have appeared to influence the work reported in this paper.

Acknowledgement

The authors gratefully acknowledge the support from the National Natural Science Foundation of China (Grant Nos. 52379103 and 52279103) and the Natural Science Foundation of Shandong Province (Grant No. ZR2023YQ049).

References

Akgül, M. A., & Ural, S. (2024). The study of mineral distribution using hyperspectral Hyperion data along the shores of Lake Salda/Türkiye. *Environmental Earth Sciences, 83*(7), 219.

Akgün, H., Muratlı, S., & Koçkar, M. K. (2014). Geotechnical investigations and preliminary support design for the Geçilmez tunnel: A case study along the Black Sea coastal highway, Giresun, northern Turkey. *Tunnelling and Underground Space Technology, 40*, 277–299.

Ali, A., Chiang, Y. W., & Santos, R. M. (2022). X-ray diffraction techniques for mineral characterization: A review for engineers of the fundamentals, applications, and research directions. *Minerals, 12*(2), 205.

Baik, H., Son, Y. S., & Kim, K. E. (2023). A tunnel coaxial 3D hyperspectral scanning system for underground mine investigation. *Scientific Reports, 13*(1), 10417.

Bhargava, A., Sachdeva, A., Sharma, K., Alsharif, M. H., Uthansakul, P., & Uthansakul, M. (2024). Hyperspectral imaging and its applications: A review. *Heliyon, 10*(12), e33208.

Bhasin, R., Barton, N., Grimstad, E., & Chryssanthakis, P. (1995). Engineering geological characterization of low strength anisotropic rocks in the Himalayan region for assessment of tunnel support. *Engineering Geology, 40*(3–4), 169–193.

Bodrito, T., Zouaoui, A., Chanussot, J., & Mairal, J. (2021). A trainable spectral-spatial sparse coding model for hyperspectral image Restoration. In *Proceedings of the the 35th International Conference on Neural Information Processing Systems (NIPS'21)* (pp. 5340–5442).

Bu, Y. Y., Zhao, Y. Q., Xue, J. Z., Kong, S. G., Yao, J. X., Chan, J. C. W., Liu, P., & Zhang, X. (2025). Transductive gradient injection for improved hyperspectral image denoising. *Engineering Applications of Artificial Intelligence, 143*, 109973.

Chang, Y., Yan, L. X., & Zhong, S. (2017). Hyper-laplacian regularized unidirectional low-rank tensor recovery for multispectral image denoising. In *Proceedings of 2017 IEEE Conference on Computer Vision and Pattern Recognition (CVPR)* (pp. 5901–5909).

Chen, C. W., Yang, H. Q., Song, K. L., Liang, D., Zhang, Y. H., & Ni, J. H. (2023). Dissolution feature differences of carbonate rock within hydro-fluctuation belt located in the Three Gorges Reservoir Area. *Engineering Geology, 327*, 107362.

Chen, T. T., Leng, C. C., Pei, Z., Peng, J. Y., & Basu, A. (2024). Multimanifold Bistructured Low Rank Representation of hyperspectral images. *Infrared Physics & Technology, 136*, 105039.

Deng, F., Pu, J., Huang, Y., & Han, Q. D. (2023). 3D geological suitability evaluation for underground space based on the AHP-cloud model. *Underground Space, 8*, 109–122.

Ducasse, E., Adeline, K., Hohmann, A., Achard, V., Bourguignon, A., Grandjean, G., & Briottet, X. (2024). Mapping of clay montmorillonite abundance in agricultural fields using unmixing methods at centimeter scale hyperspectral images. *Remote Sensing, 16*(17), 3211.

George, E. B., Ternikar, C. R., Ghosh, R., Nagesh Kumar, D., Gomez, C., Ahmad, T., Sahadevan, A. S., Gupta, P. K., & Misra, A. (2024). Assessment of spectral reduction techniques for endmember extraction in unmixing of hyperspectral images. *Advances in Space Research, 73*(2), 1237–1251.

Ghosh, P., Roy, S. K., Koirala, B., Rasti, B., & Scheunders, P. (2022). Hyperspectral unmixing using transformer network. *IEEE Transactions on Geoscience and Remote Sensing, 60*, 5535116.

Govil, H., Gill, N., Rajendran, S., Santosh, M., & Kumar, S. (2018). Identification of new base metal mineralization in Kumaon Himalaya, India, using hyperspectral remote sensing and hydrothermal alteration. *Ore Geology Reviews, 92*, 271–283.

Guo, Y. J., Lyu, S., Xiao, H. R., Liu, Y., Chen, R. F., Zhang, X. Q., Xiao, S., & Wu, G. N. (2025). Evaluation of the hygrothermal aging state of composite insulators based on hyperspectral imaging technology and the IDBO-BiGRU model. *Measurement, 253*, 117446.

He, J. P., Riley, D. N., & Barton, I. (2024). Is endmember extraction a critical step in the analysis of hyperspectral images in mining environments?. *Remote Sensing, 16*(12), 2137.

He, W., Yao, Q. M., Li, C., Yokoya, N., Zhao, Q. B., Zhang, H. Y., & Zhang, L. P. (2020). Non-local meets global: An integrated paradigm for hyperspectral image restoration. *IEEE Transactions on Pattern Analysis and Machine Intelligence, 44*(4), 2089–2107.

Huang, H. W., Wang, C. S., Zhou, M. L., & Qu, L. Q. (2024). Compressive strength detection of tunnel lining using hyperspectral images and machine learning. *Tunnelling and Underground Space Technology, 153*, 105979.

Jia, J. X., Wang, Y. M., Cheng, X. Y., Yuan, L. Y., Zhao, D., Ye, Q., Zhuang, X. Q., Shu, R., & Wang, J. Y. (2019). Destriping algorithms based on statistics and spatial filtering for visible-to-thermal infrared pushbroom hyperspectral imagery. *IEEE Transactions on Geoscience and Remote Sensing, 57*(6), 4077–4091.

Klose, C. D., Loew, S., Giese, R., & Borm, G. (2007). Spatial predictions of geological rock mass properties based on in-situ interpretations of multi-dimensional seismic data. *Engineering Geology, 93*(3–4), 99–116.

Kurz, T. H., Miguel, G. S., Dubucq, D., Kenter, J., Miegebielle, V., & Buckley, S. J. (2022). Quantitative mapping of dolomitization using close-range hyperspectral imaging: Kimmeridgian carbonate ramp, Alacón. *NE Spain. Geosphere, 18*(2), 780–799.

Liu, B., Yu, X. C., Yu, A. Z., Zhang, P. Q., & Wan, G. (2018). Spectral-spatial classification of hyperspectral imagery based on recurrent neural networks. *Remote Sensing Letters, 9*(12), 1118–1127.

Liu, F. M., Lin, P., Xu, Z. H., Shao, R. Q., & Han, T. (2023). Extraction and imaging of indicator elements for non-destructive, in-situ, fast identification of adverse geology in tunnels. *International Journal of Mining Science and Technology, 33*(12), 1437–1449.

Liu, T. X., Zhang, C. P., Li, W., Tu, S. Q., Wang, L. B., & Jin, Z. X. (2025). Face failure mechanism of fault tunnels under high-temperature and high-pressure conditions using the discrete element method. *Computers and Geotechnics, 179*, 107059.

Lobo, A., Garcia, E., Barroso, G., Martí, D., Fernandez-Turiel, J. L., & Ibáñez-Insa, J. (2021). Machine learning for mineral identification and ore estimation from hyperspectral imagery in tin–tungsten deposits: Simulation under indoor conditions. *Remote Sensing, 13*(16), 3258.

Lu, M., Zhang, J., Lyu, Q., & Zhang, L. L. (2023). Assessing the annual probability of rainfall-induced slope failure based on intensity–duration–frequency (IDF) curves. *Natural Hazards, 117*(1), 763–778.

McCormick, C. A., Corlett, H., Stacey, J., Hollis, C., Feng, J. L., Rivard, B., & Omma, J. E. (2021). Shortwave infrared hyperspectral imaging as a novel method to elucidate multi-phase dolomitization, recrystallization, and cementation in carbonate sedimentary rocks. *Scientific Reports, 11*(1), 21732.

McElderry, J. D. P., Zhu, P. Z., Mroue, K. H., Xu, J. D., Pavan, B., Fang, M., Zhao, G. S., McNerny, E., Kohn, D. H., Franceschi, R. T., Holl, M. M. B., Tecklenburg, M. M. J., Ramamoorthy, A., & Morris, M. D. (2013). Crystallinity and compositional changes in carbonated apatites: Evidence from 31P solid-state NMR, Raman, and AFM analysis. *Journal of Solid State Chemistry, 206*, 192–198.

Meng, Y., Li, G. Y., & Huang, W. (2024). Adaptive shadow compensation method in hyperspectral images via multi-exposure fusion and edge fusion. *Applied Sciences, 14*(9), 3890.

Okada, N., Maekawa, Y., Owada, N., Haga, K., Shibayama, A., & Kawamura, Y. (2020). Automated identification of mineral types and grain size using hyperspectral imaging and deep learning for mineral processing. *Minerals, 10*(9), 809.

Peng, X., Wang, P. T., Zhou, K., Yan, Z. P., Zhong, X. G., & Zhao, C. (2025). Bridge defect detection using small sample data with deep learning and Hyperspectral imaging. *Automation in Construction, 170*, 105900.

Shah, D., Trivedi, Y., Bhattacharya, B., Thakkar, P., & Srivastava, P. (2025). Hyperspectral endmember extraction using convexity based purity index. *Advances in Space Research, 75*(1), 465–480.

Son, Y. S., Noh, S. G., Bang, E. S., Kim, K. E., Cho, S. J., & Baik, H. (2022). Ground-based visible–near infrared hyperspectral imaging for monitoring cliff weathering of a volcanic island in Dokdo, South Korea. *Engineering Geology, 309*, 106854.

Tao, X. W., Paoletti, M. E., Wu, Z. Y., Haut, J. M., Ren, P., & Plaza, A. (2024). An abundance-guided attention network for hyperspectral unmixing. *IEEE Transactions on Geoscience and Remote Sensing, 62*, 5505414.

Wang, L. G., Liu, D. F., & Wang, Q. M. (2013). Geometric method of fully constrained least squares linear spectral mixture analysis. *IEEE Transactions on Geoscience and Remote Sensing, 51*(6), 3558–3566.

Wang, X. F., Wei, Y. Y., Jiang, T., Hao, F. X., & Xu, H. F. (2024a). Elastic–plastic criterion solution of deep roadway surrounding rock based on intermediate principal stress and Drucker–Prager criterion. *Energy Science & Engineering, 12*(6), 2472–2492.

Wang, Y. X., Liu, B., Wang, J. W., Meng, Q. Y., & Liu, Z. Y. (2024b). Analysis of quartz content in muck based on artificial intelligence algorithms and laser-induced breakdown spectroscopy in TBM tunneling. *Bulletin of Engineering Geology and the Environment, 83*(8), 314.

Wang, Y. Z., Cao, H. J., Chen, J., Liu, C. Q., Lu, X. J., Yin, C. X., Fu, X. H., Qiao, L., Zhang, G., Liu, C. B., Zhang, P., & Ling, Z. C. (2025). New maps of mafic mineral abundances in global mare units on the Moon. *ISPRS Journal of Photogrammetry and Remote Sensing, 224*, 348–360.

Wu, C. C., Chen, H. M., & Chang, C. I. (2012). Real-time N-finder processing algorithms for hyperspectral imagery. *Journal of Real-Time Image Processing, 7*(2), 105–129.

Xiong, F. C., Zhou, J., Zhao, Q. L., Lu, J. F., & Qian, Y. T. (2022). MAC-Net: Model-aided nonlocal neural network for hyperspectral image denoising. *IEEE Transactions on Geoscience and Remote Sensing, 60*, 1–14.

Xu, Z. H., Li, S., Lin, P., & Li, Q. J. (2025a). Non-destructive, fast and intelligent identification of coal and gangue via spatial-spectral fusion of hyperspectral images. *International Journal of Rock Mechanics and Mining Sciences, 194*, 106187.

Xu, Z. H., Li, S., Lin, P., Shi, H., & Lou, Y. F. (2025b). Partition feature extraction of hyperspectral images for in situ intelligent lithology identification. *Journal of Rock Mechanics and Geotechnical Engineering, 17*(12), 7736–7752.

Xu, Z. H., Yu, T. F., Lin, P., & Li, S. C. (2023). Adverse geology identification through mineral anomaly analysis during tunneling: Methodology and case study. *Engineering, 27*, 150–160.

Xu, Z. H., Yu, T. F., Lin, P., Wang, W. Y., & Shao, R. Q. (2022). Integrated geochemical, mineralogical, and microstructural identification of faults in tunnels and its application to TBM jamming analysis. *Tunnelling and Underground Space Technology, 128*, 104650.

Yang, L., Yang, D., Zhang, M. Y., Meng, S. W., Wang, S. L., Su, Y. T., & Xu, L. (2024). Application of nano-scratch technology to identify continental shale mineral composition and distribution length of bedding interfacial transition zone—A case study of Cretaceous Qingshankou formation in Gulong Depression, Songliao Basin, NE China. *Geoenergy Science and Engineering, 234*, 212674.

Zahiri, Z., Laefer, D. F., Kurz, T., Buckley, S., & Gowen, A. (2022). A comparison of ground-based hyperspectral imaging and red-edge multispectral imaging for façade material classification. *Automation in Construction, 136*, 104164.

Zhang, H. M., Li, X. J., Liu, J. F., Wang, Y. P., Guo, L., Wu, Z. Y., & Tian, Y. F. (2025a). A fractal characteristics analysis of the pore throat structure in low-permeability sandstone reservoirs: A case study of the Yanchang formation, Southeast Ordos Basin. *Fractal and Fractional, 9*(4), 224.

Zhang, J., Sun, Y., Hu, J. Z., & Huang, H. W. (2023). Assessing site investigation program for design of shield tunnels. *Underground Space, 9*, 31–42.

Zhang, T. H., Zhao, J. L., Fang, S., Li, Z., Zhang, Q., & Gong, M. G. (2025b). Hyperspectral image restoration via the collaboration of low-rank tensor denoising and completion. *Pattern Recognition, 165*, 111629.

Zhao, L. L., Hong, H. L., Liu, J. C., Fang, Q., Yao, Y. Z., Tan, W., Yin, K., Wang, C. W., Chen, M., & Algeo, T. J. (2018). Assessing the utility of visible-to-shortwave infrared reflectance spectroscopy for analysis of soil weathering intensity and paleoclimate reconstruction. *Palaeogeography, Palaeoclimatology, Palaeoecology, 512*, 80–94.

Zhou, H., Zhang, C. Q., Li, Z., Hu, D. W., & Hou, J. (2014). Analysis of mechanical behavior of soft rocks and stability control in deep tunnels. *Journal of Rock Mechanics and Geotechnical Engineering, 6*(3), 219–226.